applied optics

Super-resolution imaging of photonic crystals using the dual-space microscopy technique

Darshan B. Desai,[1,2,*] Sanchari Sen,[1,2] Maksym V. Zhelyeznyakov,[1] Wedad Alenazi,[1] and Luis Grave de Peralta[1,2]

[1]Department of Physics, Texas Tech University, Lubbock, Texas 79409, USA
[2]NanoTech Center, Texas Tech University, Lubbock, Texas 79409, USA
*Corresponding author: darshan.desai@ttu.edu

Received 17 March 2016; accepted 13 April 2016; posted 18 April 2016 (Doc. ID 261412); published 12 May 2016

We present an experimental implementation of the recently proposed dual-space microscopy (DSM), an optical microscopy technique based on simultaneous observation of an object in the position and momentum spaces, using computer-controlled hemispherical digital condensers. We demonstrate that DSM is capable of resolving structures below the Rayleigh resolution limit.

OCIS codes: (110.0180) Microscopy; (100.0100) Image processing.

http://dx.doi.org/10.1364/AO.55.003929

1. INTRODUCTION

Microscope condensers provide inclined illumination that permits an increase of the resolution of optical microscopes of only up to the Rayleigh resolution limit [1–5], which means that if λ is the vacuum wavelength of the light used to illuminate a sample using a traditional condenser, and if the light transmitted through the sample is collected by an objective lens with a numerical aperture NA_o, then, according to Abbe's theory of image formation [6–8], the minimum period observable ($p_{\min}$) with this setup is limited to $p_{\min} \sim \lambda/(2\mathrm{NA}_o)$. Also, with conventional single-shot imaging techniques, the phase induced in the light that is transmitted through the sample cannot be recovered. However, digitally controlling the illumination from a condenser, as with hemispherical digital condensers (HDCs) [9,10], permits the implementation of Fourier ptychographic microscopy (FPM), which is based on calculating a large synthetic numerical aperture ($\mathrm{NA}_s > \mathrm{NA}_o$) in the Fourier plane (FP) from the acquired low resolution far-field real plane (RP) intensity images of the light transmitted through a sample that is illuminated at various angles [11–15]. Simultaneously, FPM permits us to recover the experimentally unmeasured phase that gets induced in the light transmitted through the sample [11–16]. Nevertheless, we recently demonstrated that for samples containing a single periodic structure with a period $p < \lambda/(2\mathrm{NA}_o)$, as for photonic or plasmonic crystals, the FPM phase-recovery algorithm fails to correctly resolve the periodicity of the sample [16]. This is because in none of the low resolution RP intensity images acquired using a microscope objective with NA_o is a single periodic structure with $p < \lambda/(2\mathrm{NA}_o)$ visible. However, the experimentally acquired FP intensity images associated with these low resolution RP intensity images contain the first-order diffraction spots corresponding to the correct spatial periodicity [10]. Detection methods based on FP intensity images of photonic and plasmonic crystals with $p < \lambda/(2\mathrm{NA}_o)$ have been reported [15,17,18]. Recently, we proposed a novel imaging technique called dual-space microscopy (DSM), which is based on simultaneously obtaining RP and FP intensity images of the sample, and then processing all the experimentally obtained images using a phase-recovery iterative algorithm to resolve periodic and nonperiodic structures well below the Rayleigh resolution limit [19]. In this work, for the first time, we experimentally implement the DSM technique using a computer-controlled HDC to study the lateral resolution of the RP intensity images obtained using the DSM technique. The computer-controlled HDC used in this work consists of 64 light emitting diodes (LEDs) that are uniformly distributed on the internal surface of a hemisphere [10,15] and can be used to illuminate the sample with controllable directional light with superior illumination uniformity in comparison to the condensers with a planar array of LEDs [11,12], as the LEDs are at the same distance from the sample. This paper is organized as follows: in Section 2, we discuss the structure and fabrication of the sample and the imaging setup used in the experiments described in this paper. The DSM algorithm is described in Section 3. In Section 4, we demonstrate experimental implementation of the DSM technique using HDCs. In Section 5, we demonstrate the capability of DSM technique for imaging below the Rayleigh resolution limit. Finally, conclusions of this work are presented in Section 6.

2. EXPERIMENTAL SETUP AND SAMPLE STRUCTURE

A. Experimental Setup

The microscope arrangement used for implementing the DSM technique is as shown in Fig. 1(a). We used a commercially available Nikon Ti inverted microscope and replaced its built-in illumination source with the HDC, whose photograph is shown in Fig. 1(b). The HDC was centered over the area of interest of the sample, so that all 16 LEDs in each of the four circular rows correspond to a condenser numerical aperture of $NA_c \sim 0.58$, ~0.73, ~0.89, and ~0.97 [10,15]. Each of the 64 LEDs of the HDC can be turned on and off independently to illuminate the sample. An objective lens with $NA_o = 0.8$ was used to collect the light transmitted through the sample. The light collected by the objective lens was filtered at $\lambda = 450$ nm, the LEDs' peak emissivity wavelength [10], by placing a spectral bandpass filter (having 10 nm bandwidth) beneath the objective lens. Finally, two charge-coupled device cameras were used to capture the RP $(a_j(r)^2)$ and FP $(A_j(k)^2)$ intensity images of the sample.

B. Sample Structure

In order to obtain quantitative evaluation of the resolution of the obtained RP images, we used periodic structures of chromium (Cr) pillars arranged with rectangular lattice symmetry; two different periodicities, p_x and p_y, in two mutually perpendicular directions; and pillar diameter $d = p_y/2$. We fabricated two different samples, one of them with periodicities $p_x = 500$ nm and $p_y = 300$ nm, and another with periodicities $p_x = 600$ nm and $p_y = 270$ nm [15]. The process of creating the periodic structures starts with spin-coating a ~100 nm thick layer of poly methyl-methacrylate (PMMA) over a ~150 μm thick glass coverslip, and then thermally evaporating a ~10 nm thick Al layer, which results in a structure that can be used for e-beam lithography. After lithographic patterning, hydrofluoric acid was used to etch away the Al layer, and a methyl-isobutyl-ketone and isopropanol solution was used to etch out the parts of PMMA exposed to the electron beam during lithography, thereby forming holes in the PMMA layer arranged in a rectangular lattice pattern. A ~15 nm thick Cr layer was then deposited on top of the PMMA layer, which gets filled in the holes in the previously revealed lattice arrangement. Finally, the sample was sonicated in acetone and then in isopropanol, to dissolve the PMMA layer, thereby leaving only a periodic structure formed by Cr pillars.

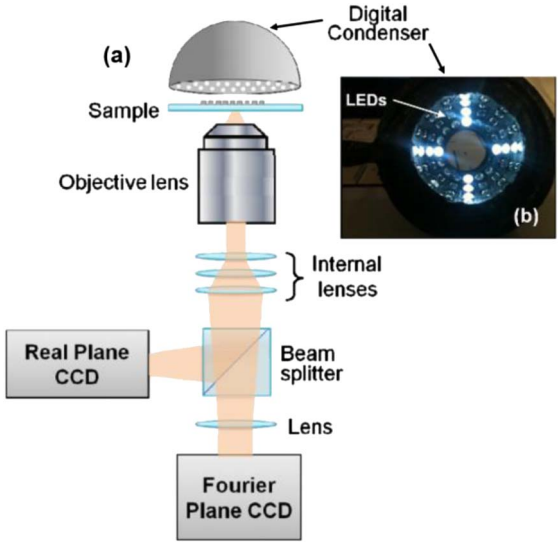

Fig. 1. (a) Schematic diagram of the experimental setup. (b) Inner view of the HDC light source.

3. DSM ALGORITHM

The DSM algorithm used in this work, and sketched in Fig. 2, is a two-dimensional (2D) version of the 1D-DSM algorithm described in [19]. As shown in the block (1) in Fig. 2, like in FPM [11], the DSM algorithm could start, for instance, assuming amplitude $[a_{m=0}(r)]$ and phase $[p_{m=0}(r)]$ identically equal to one and zero, respectively, as the initial approximation $(m = 0)$ corresponding to the high resolution RP intensity image $[a_{m=0}(r)^2]$. Then, as shown in the block (2) in Fig. 2, the first actual approximation $(m = 1, j = 1)$ of the amplitude and phase corresponding to the FP image with large NA_s is calculated by applying a 2D Fourier transform operation (F) [8]:

$$A^{\text{act}}_{m,j}(k)e^{iP^{\text{act}}_{m,j}(k)} = F[a_{m=0}(r)e^{ip_{m=0}(r)}]. \quad (1)$$

As shown in the block (3) in Fig. 2, this follows by the use of Eq. (2) to calculate the first approximation to the amplitude $[A_{m=1,j=1}(k)]$ and phase $[P_{m=1,j=1}(k)]$ corresponding to the FP image with small $NA_o[A_{m,j}(k)^2]$ that would be observed by illuminating the sample with the LED number j:

$$A_{m,j}(k)e^{iP_{m,j}(k)} = A^{\text{act}}_{m,j}(k - k_j)e^{iP^{\text{act}}_{m,j}(k-k_j)} \cdot W_o. \quad (2)$$

In Eq. (2), $k_j = (2\pi/\lambda)\text{NA}_c$, where NA_c takes the value corresponding to the LED number j, and W_o is a circular window of radius NA_o, amplitude equal to one, and centered at $k = 0$. At this point, as shown in the blocks (4) and (5) in Fig. 2, the calculated amplitude of the FP image with small $NA_o[A_{m,j}(k)]$ is substituted by the amplitude of the corresponding experimental FP image $[A_j(k)]$, which was obtained as described in Section 2. This is in contrast with FPM, where no experimental FP images are used [11–14,16,19]. In the next step, as shown in the block (6) in Fig. 2, the amplitude $[a_{m,j}(r)]$ and phase $[p_{m,j}(r)]$ corresponding to the related low resolution RP image are calculated by applying a 2D inverse Fourier transform operation (F^{-1}):

$$a_{m,j}(r)e^{ip_{m,j}(r)} = F^{-1}[A_j(k)e^{iP_{m,j}(k)}]. \quad (3)$$

At this point, as shown in the blocks (7) and (8) in Fig. 2, like in FPM, in DSM, the calculated amplitude of the low resolution RP image $[a_{m,j}(r)]$ is substituted by the amplitude of the corresponding experimental low resolution RP image $[a_j(r)]$, which was obtained as described in Section 2. Then, as shown in the block (9) in Fig. 2, the amplitude and phase corresponding to the FP image with NA_o is recalculated using the following equation:

$$A^{\text{rec}}_{m,j}(k)e^{iP^{\text{rec}}_{m,j}(k)} = F[a_j(r)e^{ip_{m,j}(r)}] \cdot W_o. \quad (4)$$

Finally, as shown in the block (10) in Fig. 2, the updated approximations of the amplitude and phase corresponding to the synthetic numerical aperture are calculated by first shifting the

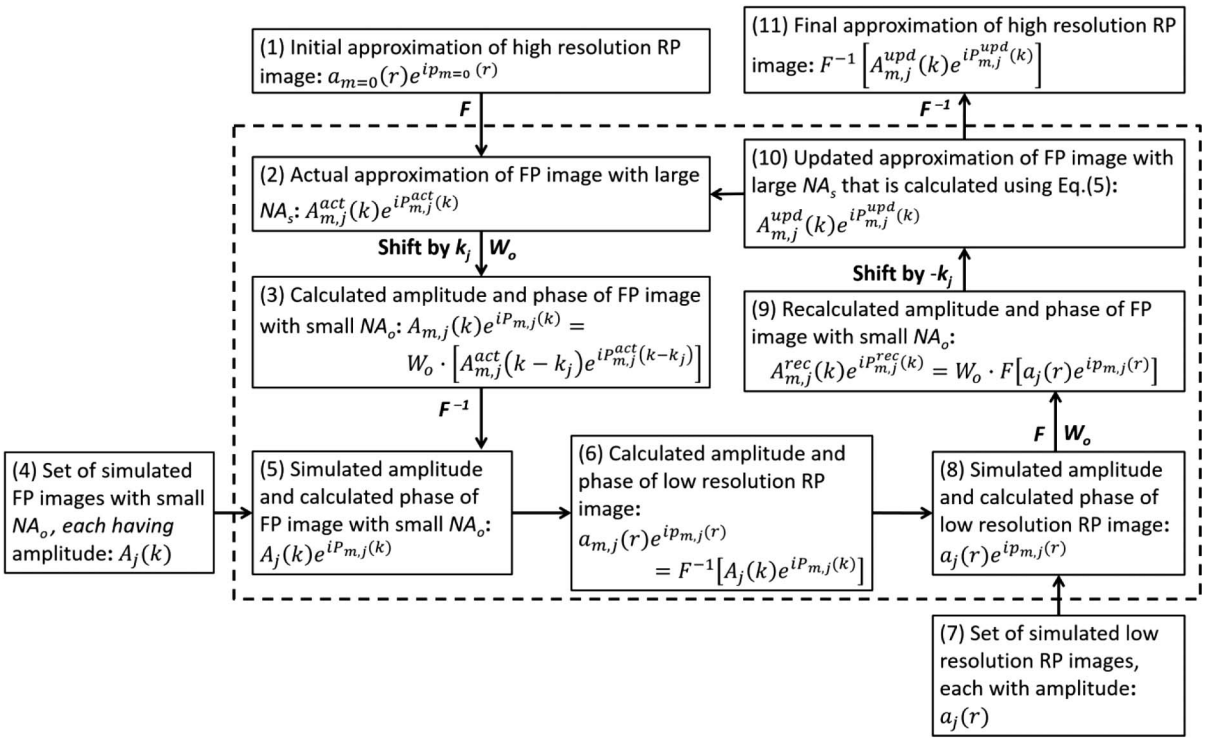

Fig. 2. DSM phase-recovery algorithm. The part of the algorithm included in the box with the discontinuous line is repeated for NA_c corresponding to each LED, which constitutes one complete iteration. The algorithm converges after several iterations.

complex functions corresponding to the calculated and recalculated FP images with small NA_o by the amount $-k_j$, and then adding a weighted difference between them to the complex function corresponding to the actual approximations of the synthetic numerical aperture; that is, using Eq. (5),

$$A^{\mathrm{upd}}_{m,j}(k)e^{iP^{\mathrm{upd}}_{m,j}(k)} = A^{\mathrm{act}}_{m,j}(k)e^{iP^{\mathrm{act}}_{m,j}(k)} + \alpha[A^{\mathrm{rec}}_{m,j}(k+k_j)e^{iP^{\mathrm{rec}}_{m,j}(k+k_j)} - \gamma A_{m,j}(k+k_j)e^{iP_{m,j}(k+k_j)}]. \quad (5)$$

In this work we used the weighting parameter values $\alpha = 1$ and $\gamma = 0$. As shown by the arrow between blocks (10) and (2) in Fig. 2, after the initial approximation of the FP image with large NA_s is updated, the amplitude and phase corresponding to the updated FP image with NA_s are used as the actual approximation of them ($j = 2$). The operations included in the box with the discontinuous line in Fig. 2 are successively done for each pair of experimental low resolution RP image and corresponding FP image with small NA_o (indicated by sub-index j). This constitutes the first iteration ($m = 1$) in the FPM algorithm, and the algorithm should converge after several iterations. Finally, as shown in the block (11) in Fig. 2, the 2D Fourier transform of the complex function corresponding to the updated FP image with large NA_s gives the amplitude and phase corresponding to the final high resolution RP image. We found that, typically, convergence occurs after few dozen iterations, but in order to be sure that we did not miss any important development, we explored the algorithm results even after hundreds of iterations without finding significant differences from the results obtained at convergence.

4. EXPERIMENTAL IMPLEMENTATION OF THE DSM TECHNIQUE USING HDC

The DSM technique uses a set of low resolution RP images and the corresponding set of FP images obtained by illuminating the sample obliquely. In this work, these images were obtained experimentally by illuminating the sample with each of the 64 LEDs of HDC using the experimental arrangement sketched in Fig. 1(a), and an objective lens with $NA_o = 0.8$. To first approximation, the light from each of these LEDs can be assumed to be a coherent monochromatic plane wave that is obliquely incident over the sample surface, and hence, when using a condenser numerical aperture of $NA_c \le NA_o$, $p_{\min}$ is given by the following equation [2,4,9,15]:

$$p_{\min} \approx \frac{\lambda}{NA_o + NA_c}. \quad (6)$$

According to Abbe's theory of image formation, for any spatial periodicity less than the Rayleigh resolution limit but larger than the minimum observable period ($p_{\min}$) in Eq. (6), when condenser numerical aperture of $NA_c > NA_o$ is used, the acquired low resolution RP image will not show the periodicity of the sample, but the associated FP image may contain a diffraction spot corresponding to correct periodicity in the sample [10,15]. For experimental implementation of DSM technique, we used the sample with $p_x = 500$ nm and $p_y = 300$ nm periodicities in two mutually perpendicular directions as the object under observation. The Rayleigh resolution limit for this experimental setup was calculated to be ~281 nm, and thus, we investigate the performance of DSM technique for a periodicity that is slightly greater than the Rayleigh resolution limit.

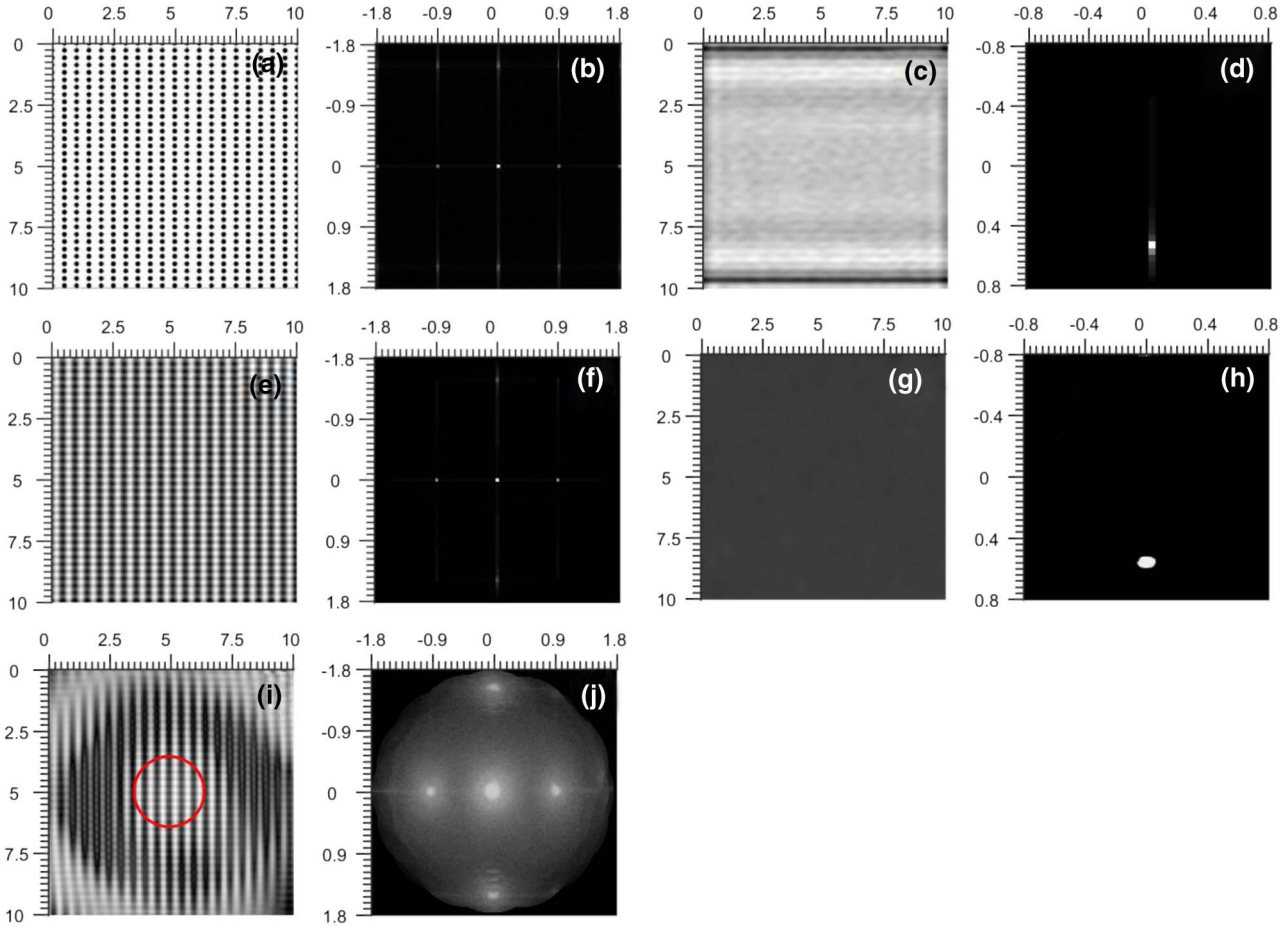

Fig. 3. [(a), (b)] Pairs of RP and FP intensity images of a sample with $p_x = 500$ nm and $p_y = 300$ nm, respectively, that mimic the object under observation in the microscope; [(e), (f) and (i), (j)] are reconstructed with the DSM algorithm by using all [(e), (f)] computer-generated images that mimic image acquisition in the microscope, and [(i), (j)] experimentally acquired images. [(c), (d) and (g) (h)] Pairs of low resolution RP images and corresponding FP images with small $\mathrm{NA}_o = 0.8$ that are created [(c), (d)] from simulated object intensity shown in (a), and [(g), (h)] from experimentally acquired images, which are obtained using $\mathrm{NA}_c = 0.97$.

Also, in order to validate the experiment, we created simulated low resolution RP and FP images that mimic the experimentally acquired RP and FP images. The simulation was conducted using a 2D extension of a 1D simulation algorithm previously reported in Refs. [16,19]. We first defined the complex function $a(r)e^{ip(r)}$ describing the optical disturbance at the object plane [8,16,19]. The corresponding intensity at the object plane $(a(r)^2)$ is shown in Fig. 3(a). The phase $(p(r))$ was also chosen with the same periodicities as the intensity (not shown). The modulus-squared $(A(k)^2)$ of the 2D Fourier transform of $a(r)e^{ip(r)}$ $(A(k)e^{iP(k)})$ is shown in Fig. 3(b) where, for convenience, the wave-number $k = (2\pi/\lambda)\mathrm{NA}$ is represented in units of numerical aperture $(\mathrm{NA} = \lambda k/2\pi)$. The complex function $A(k)e^{iP(k)}$ was then used to obtain the set of simulated FP images with small NA_o that could be observed at the microscope's FP. Each FP image with small NA_o was simulated by cropping the function $A(k - k_c)e^{iP(k-k_c)}$ to a disc of radius NA_o that is centered at $k = 0$, as described in Refs. [16,19]. The corresponding low resolution RP images were then obtained by 2D Fourier transform of these FP images with small NA_o. For instance, the low resolution RP image and the corresponding FP image with $\mathrm{NA}_o = 0.8$ that were simulated using $\mathrm{NA}_c = 0.97$ are shown in Figs. 3(c) and 3(d), respectively. The two sets of FP images with small NA_o and the corresponding low resolution RP images were then processed using the DSM algorithm described in Section 2, to obtain the high resolution RP intensity image shown in Fig. 3(e), and the corresponding synthetic FP intensity image with $\mathrm{NA}_s = 0.97 + 0.8 = 1.77$ shown in Fig. 3(f). Comparison of the high resolution RP intensity image shown in Fig. 3(e) with the exact optical disturbance intensity at the object plane shown in Fig. 3(a) suggests that the DSM algorithm worked correctly. This is further supported by the correct locations $\lambda/p_x = 1.5$ and $\lambda/p_y = 0.9$ of the first order diffraction spots in Fig. 3(f). Also, on comparing Figs. 3(b) and 3(f), we notice that although the number of diffraction spots in obtained FP intensity image with $\mathrm{NA}_s = 1.77$ shown in Fig. 3(f) is higher than in any of the simulated FP images with small $\mathrm{NA}_o = 0.8$ [Fig. 3(d)], the number of diffraction spots have to be less than those in Fig. 3(b) due to the finite value of NA_s, which explains the minor differences in the resolution of the intensity distribution shown in Fig. 3(a) and the high resolution RP intensity image shown in Fig. 3(e). On the other hand, Figs. 3(i) and 3(j) show the high resolution RP image and

the synthetic FP image, respectively, that were obtained by processing the experimentally acquired RP and FP images using the DSM algorithm. An instance of a pair of low resolution RP image and the corresponding FP image with $NA_o = 0.8$ that were experimentally acquired by illuminating the sample with a LED with $NA_c = 0.97$ is shown in Figs. 3(g) and 3(h), respectively. The position of the diffraction spots in the FP image with $NA_s = 1.77$ shown in Fig. 3(j) are in the same position as in the FP images shown in Figs. 3(b) and 3(f). This is in excellent correspondence with the observation of the correct periodicities in the small field-of-view (FOV) confined in the red circle added to the high resolution RP intensity image shown in Fig. 3(i). Such small effective FOV is a consequence of the repetitive use of Fourier transforms in the phase-recovery algorithm, which assumes that LED emits a plane-wave to illuminate the sample [11,12]. This is in agreement with the extremely small size of the diffraction spots in the simulated FP images shown in Figs. 3(d) and 3(f). In reality, LEDs emits a divergent beam of light, and therefore, an additional non-zero intrinsic numerical aperture ($NA_{LED} \neq 0$) could be associated to each LED. From the radius of the diffraction spots in the FP experimental images [Fig. 3(h)], we estimated an average value of $NA_{LED} \sim 0.05$ for the LEDs in the HDC. This value of NA_{LED} represents the actual minimum resolvable feature in each of the experimental FP images and in the FP image with $NA_s = 1.77$ shown in Fig. 3(j). Consequently, the radius (R_{DSM}) of the circular effective field-of-view of the high resolution RP intensity image obtained using the DSM technique (FOV_{DSM}) was calculated using the following equation:

$$R_{DSM} \approx \frac{\lambda}{2\pi NA_{LED}}. \quad (7)$$

Using Eq. (7), we estimated $R_{DSM} \sim 1.4$ μm, which matches the diameter of the red circle added to Fig. 3(i). It should be noted that the undesirably small FOV_{DSM} could be increased by illuminating the sample with a laser beam with much smaller intrinsic numerical aperture. The results shown in Fig. 4 highlight the advantages of DSM in respect to FPM. No periodicity is visible in any of the dark-field ($NA_c > NA_o$) low resolution RP image that is simulated or experimentally obtained with $NA_c = 0.89$ and 0.97 [Figs. 3(c) and 3(g)] [15,16]. This is because in the corresponding FP images with $NA_o = 0.8$ only a first-order diffraction spot corresponding to the sample's periodicities is visible [Figs. 3(d) and 3(h)] [15,16]. Consequently, the high resolution RP images obtained with the FPM algorithm, and using only all simulated or experimental dark-field low resolution RP images, also show no periodicity (not shown) [15,16]. However, both periodicities are clearly observed in the high resolution RP image obtained with the DSM algorithm, and using only all simulated [Fig. 4(a)] or experimental [Fig. 4(c)] dark-field low resolution RP images. This is in excellent correspondence with the diffraction spots observed in the corresponding synthetic FP images shown in Figs. 4(b) and 4(d), respectively. Here, again, although the FOV_{DSM} is small because $NA_{LED} \sim 0.05$, the correct periodicities are observed inside the circular effective field of view represented by the red circle added to the high resolution RP intensity image shown in Fig. 4(c). The small size of FOV_{DSM} corresponds with the larger size of the diffraction spots in the synthetic FP image shown in Fig. 4(d) when compared with the diffraction spots in Fig. 4(b).

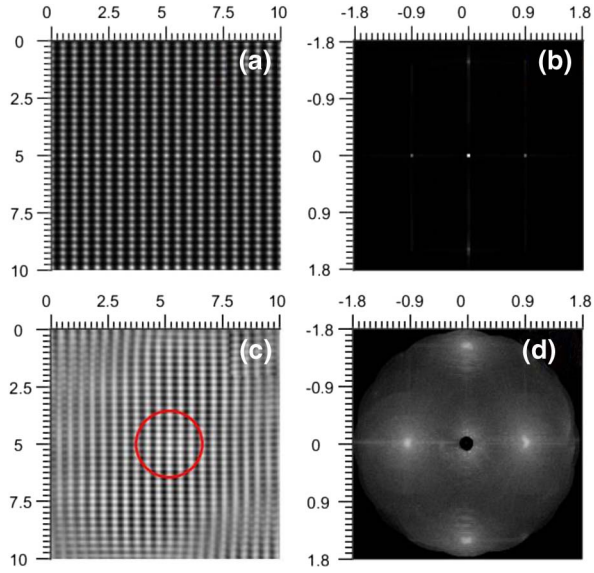

Fig. 4. Pairs of RP and FP images of a sample with $p_x = 500$ nm and $p_y = 300$ nm showing the reconstructed intensity images obtained with DSM algorithm by using [(a), (b)] computer-generated images that mimic image acquisition in microscope, and [(c), (d)] experimentally acquired images, which were obtained with $NA_o = 0.8$, and $NA_c = 0.89$ and $NA_c = 0.97$ only.

5. IMAGING BELOW THE RAYLEIGH RESOLUTION LIMIT USING THE DSM TECHNIQUE

After exploring implementation of DSM technique with HDC using a sample having periodicities slightly above the Rayleigh resolution limit, we used a sample with periodicities $p_x = 600$ nm and $p_y = 270$ nm for demonstrating the predicted capability of DSM technique for resolving single periodic structures with a period in the range $\lambda/(2NA_o) = 281$ nm $> p > \lambda/(NA_o + NA_c) = 254$ nm [19]. It has been previously reported that FPM fails to resolve the 270 nm periodicity of such sample [15,16]. Figures 5(a) and 5(b) show the high resolution RP and the corresponding synthetic FP images, respectively, obtained by processing all simulated low resolution RP images and corresponding FP images using the DSM algorithm. The obtained high resolution RP image for the sample in Fig. 5(a) clearly reveals the $p_y = 270$ nm periodicity, which suggests that the DSM technique can resolve a single periodic structure with a period below the Rayleigh resolution limit. On the other hand, Fig. 5(c) shows the useful FOV_{DSM} of the high resolution RP image obtained by processing the experimental RP and FP images using the DSM algorithm. The poor contrast of the sample's smallest periodicity in Fig. 5(c) can be explained by the presence of unwanted reflections in the corresponding synthetic FP image shown in Fig. 5(d). The unwanted reflections occur at the internal surface of the HDC dome; therefore, both undesirable features, the small size of FOV_{DSM} and the unwanted reflections, could be simultaneously eliminated by substituting the HDC by a single laser beam and a system

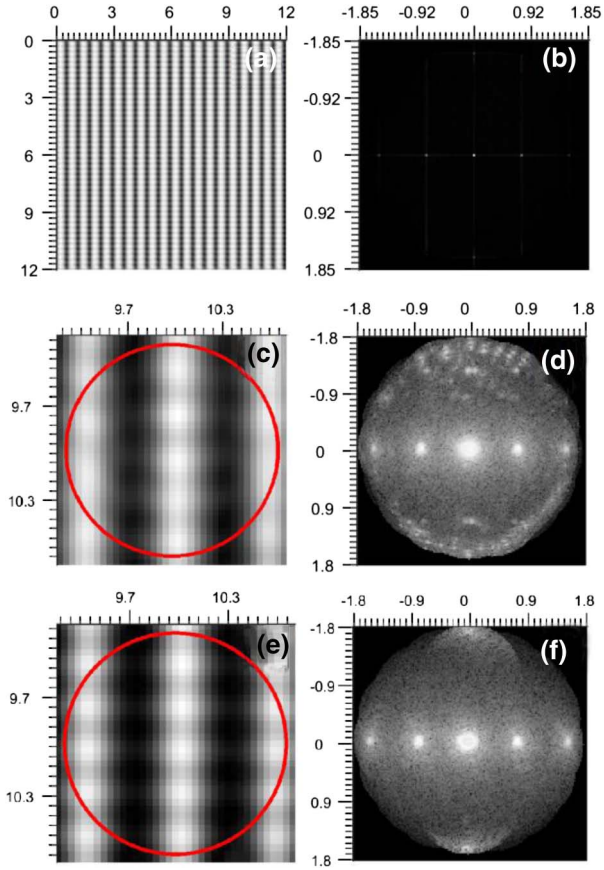

Fig. 5. Pairs of RP and FP intensity images of a sample with $p_x = 600$ nm and $p_y = 270$ nm that were reconstructed with DSM algorithm by using all [(a), (b)] computer-generated images that mimic image acquisition in the microscope, and (c–f) experimentally acquired images, which were obtained with $NA_o = 0.8$. The reconstructed intensity images shown in [(c), (d)] are obtained using the HDC microscope setup in Fig. 1(a), and images shown in [(e), (f)] are obtained by removing reflections appearing in (d) by using simple image post-processing methods. The RP images in (c) and (e) are cropped to show only useful FOV_{DSM}.

for changing the incidence angle of the beam on the sample. Using image post-processing methods, we removed the unwanted reflections from the experimental FP images. As shown in Fig. 5(e), both periodicities of the sample are observed in the useful FOV_{DSM} of the high resolution RP image that was obtained with the DSM algorithm using the post-processed experimental FP images. This is further supported by the correct location of the first order diffraction spots in the corresponding synthetic FP image shown in Fig. 5(f). The observation of the 270 nm periodicity in Fig. 5(e) demonstrates the capability of DSM for producing images with a resolution better than the Rayleigh resolution limit.

6. CONCLUSIONS

We presented the first experimental implementation of the DSM technique using a HDC. We experimentally confirmed that the DSM technique can image photonic crystals with a period smaller than the Rayleigh resolution limit. We identified the undesirably small size of FOV_{DSM} to be a consequence of the divergent emission of light from LEDs. Considering that the super-resolution capabilities of DSM when observing nonperiodic samples have been predicted [19], we expect that implementation of the DSM technique using a highly collimated laser beam will result in a practical super-resolution technique for imaging periodic and nonperiodic samples.

REFERENCES

1. H. Köheler, "On Abbe's theory of image formation in the microscope," Opt. Acta **28**, 1691–1701 (2010).
2. H. H. Hopkins and P. M. Barham, "The influence of the condenser on microscopic resolution," Proc. Phys. Soc. B **63**, 737–744 (1950).
3. A. Vainrub, O. Pustovyy, and V. Vodyanoy, "Resolution of 90 nm (λ/5) in an optical transmission microscope with annular condenser," Opt. Lett. **31**, 2855–2857 (2006).
4. D. B. Desai, D. Dominguez, A. A. Bernussi, and L. Grave de Peralta, "Ultra-thin condensers for optical subwavelength resolution microscopy," J. Appl. Phys. **115**, 093103 (2014).
5. D. B. Desai and L. Grave de Peralta, "Optical condensers formed in wet-mounting setup," Appl. Opt. **54**, 3580–3587 (2015).
6. E. Hecht, *Optics*, 3rd ed. (Addison Wesley, 1998).
7. M. Born and E. Wolf, *Principles of Optics*, 5th ed. (Pergamon, 1975).
8. J. W. Goodman, *Introduction to Fourier Optics* (McGraw-Hill, 1968).
9. D. Dominguez, L. Molina, D. B. Desai, T. O'Loughlin, A. A. Bernussi, and L. Grave de Peralta, "Hemispherical digital optical condensers with no lenses, mirrors, or moving parts," Opt. Express **22**, 6948–6957 (2014).
10. S. Sen, L. Molina, D. Cao, D. B. Desai, A. A. Bernussi, and L. Grave de Peralta, "Versatile optical microscopy using a reconfigurable hemispherical digital condenser," Biomed. Opt. Express **6**, 658–667 (2015).
11. G. Zheng, R. Horstmeyer, and C. Yang, "Wide-field, high-resolution Fourier ptychographic microscopy," Nat. Photonics **7**, 739–745 (2013).
12. L. Tian, X. Li, K. Ramchandran, and L. Waller, "Multiplexed coded illumination for Fourier ptychography with LED array microscope," Biomed. Opt. Express **14**, 3093 (2014).
13. K. Guo, S. Dong, P. Nanda, and G. Zheng, "Optimization of sampling pattern and the design of Fourier ptychographic illuminator," Opt. Express **23**, 6171 (2015).
14. X. Ou, R. Horstmeyer, G. Zheng, and C. Yang, "High numerical aperture Fourier ptychography: principle, implementation and characterization," Opt. Express **23**, 3473 (2015).
15. S. Sen, D. B. Desai, M. Alsubaie, M. Zhelyeznyakov, L. Molina, H. Sari-Sarraf, A. A. Bernussi, and L. Grave de Peralta, "Imaging photonic crystals using Fourier plane imaging and Fourier ptychographic microscopy techniques implemented with a computer-controlled hemispherical digital condenser," Opt. Commun. (to be published).
16. D. B. Desai, H. Sari-Sarraf, A. A. Bernussi, and L. Grave de Peralta, "One-dimensional simulation of Fourier ptychographic microscopy," J. Opt. Soc. Am. A (to be published).
17. D. B. Desai, M. M. S. Aldawsari, B. M. H. Alharbi, S. Sen, and L. Grave de Peralta, "Comprehensive study of unexpected microscope condensers formed in sample arrangements commonly used in optical microscopy," Appl. Opt. **54**, 7781–7788 (2015).
18. D. Dominguez, M. Alhusain, N. Alharbi, A. A. Bernussi, and L. Grave de Peralta, "Fourier plane imaging microscopy for detection of plasmonic crystals with periods beyond the optical diffraction limit," Plasmonics **10**, 1337–1344 (2015).
19. D. B. Desai, S. A. S. Alanzi, and L. Grave de Peralta, "Dual-space microscopy," Opt. Express (to be published).